Available online at www.sciencedirect.com
ScienceDirect
Comput. Methods Appl. Mech. Engrg. 384 (2021) 113958
Computer methods in applied mechanics and engineering
www.elsevier.com/locate/cma

Three-dimensional transient heat conduction problems in FGMs via IG-DRBEM

Bo Yu[a,*], Geyong Cao[a], Zeng Meng[a], Yanpeng Gong[b], Chunying Dong[c]

[a] *School of Civil Engineering, Hefei University of Technology, Hefei 230009, PR China*
[b] *Institute of Electronics Packaging Technology and Reliability, Faculty of Materials and Manufacturing, Beijing University of Technology, Beijing, 100124, PR China*
[c] *Department of Mechanics, School of Aerospace Engineering, Beijing Institute of Technology, Beijing, 100081, PR China*

Received 23 January 2021; received in revised form 25 April 2021; accepted 23 May 2021
Available online 8 June 2021

Abstract

In this paper, the isogeometric dual reciprocity boundary element method (IG-DRBEM) is firstly applied to solve three-dimensional (3D) transient heat conduction problems in functionally graded materials (FGMs) with heat sources. Using the fundamental solution of the 3D potential problem, the integral equation of boundary-domain is established by the weighted residual method. The normalized temperature is introduced, and the domain integral is transformed into the boundary integral by the dual reciprocity method (DRM). Finally, the theoretical framework of the isogeometric BEM for FGMs problems is established. Furthermore, the effects of different approximation functions, time steps, element refinements and the distance from the inner point to the boundary on the results are discussed in detail via several examples, which verify the validity of the presented method. In order to promote the development of IGBEM, the program code of this article can be obtained by sending email to yubochina@hfut.edu.cn.

Keywords: Isogeometric BEM; Dual reciprocity method; Functionally graded materials; Transient heat transfer

1. Introduction

Functionally graded materials (FGMs) have been applied in high-end manufacturing, aerospace and other fields since they were proposed last century due to their excellent mechanical and heat transfer characteristics. For example, in order to improve the thermal protection performance of flight devices, FGMs are usually coated on the surface of the devices. Therefore, the study of transient heat transfer problems of FGMs can provide effective parameters for the development of equipment and save cost to a certain extent.

There are many numerical methods to analyze transient heat transfer problems, among which the boundary element method (BEM) is one of the most effective methods. Since the isogeometric boundary element method (IGBEM) [1] was proposed in 2012, it has been favored by more and more researchers. Compared with the isogeometric finite element method [2], the IGBEM can directly use CAD model information, without the need to

* Corresponding author.
E-mail address: yubochina@hfut.edu.cn (B. Yu).

https://doi.org/10.1016/j.cma.2021.113958
0045-7825/

discretize the inner domain. Therefore, the IGBEM achieves seamless connection from CAD to CAE well, which avoids the process of element discretization and saves cost to a certain extent.

So far, IGBEM has been applied in many fields. For example, using the Non-Uniform Rational B-Splines (NURBS) [1,3] and the unstructured T-splines [4] solved the two-dimensional (2D) and three-dimensional (3D) linear elastostatic problem, respectively. Meanwhile, the IGBEM was also extended to solve the Helmholtz problem [5–7], the wave-resistance problem [8], the elasto-plastic problem [9,10], the crack problem [11–14], the shape optimization problem [15–18], the topology optimization [19,20], the 3D potential problem [21] and the heat transfer problem [22,23]. It is worth noting that most of the problems solved by IGBEM are for steady and homogeneous materials. More recently, Yu et al. [23] proposed the isogeometric dual reciprocity BEM (IG-DRBEM) to analyze the 2D transient heat transfer problem of homogeneous material. Similar to traditional BEM, domain integrals will be generated in the integral equation when the transient heat transfer problem is solved due to using the common steady fundamental solution especially involving heterogeneous materials.

The realization of fast transformation from the domain integral to the boundary integral is directly related to the maintenance of dimension reduction advantage of BEM. Many transformation methods of domain integral have been proposed in using BEM such as the dual reciprocity method (DRM) [24,25], the multiple reciprocity method (MRM) [26,27], the triple-reciprocity BEM [28–30] and the radial integration method (RIM) [31,32]. In the above several methods, in order to achieve the common purpose of transforming domain integrals into boundary integrals, MRM introduces a sequence of higher-order fundamental solutions of the Laplace operator and repeatedly applies the reciprocity theorem. Since no interior nodes are required, MRM has superior boundary-only characteristics over DRM. The fast convergence of the higher-order fundamental solutions ensures that the infinite series can be calculated by several truncated terms, but the truncated error leads to the numerical instability of MRM, and the calculation of the higher-order fundamental solutions becomes difficult in the recurrence formula governed by the Laplace operator. Similar to DRM, the triple-reciprocity BEM first approximates the nonhomogeneous term with the radial basis functions and then eliminates the domain integral in the boundary integral equation with the reciprocity theorem. Although triple-reciprocity BEM only uses the low-order fundamental solution, the performance of its approximate particular solution is poor and its reliability is lower than that of DRM. RIM is based on pure mathematical treatment and can be used to transform any domain integral to boundary integral without using the Laplace operator and the particular solution of the problem, but it is more complex to derive and program and is not as easy to implement as DRM. As for DRM, although it is always necessary to distribute some nodes in the domain to ensure convergence spoils the elegance of the boundary-type methods, and for domain integral consisting of known functions, approximate functions are still required, which loses some precision. However, since DRM uses the same fundamental solution as the steady-state homogeneous problem without the need for higher-order fundamental solutions, the coefficient matrices can be directly used to solve the transient nonhomogeneous problem after the steady-state problem is completed, so DRM has a better matrix structure and is easier to implement. Up to now, the dual reciprocity BEM (DRBEM) which is formed by combining DRM with BEM has been applied to solve the structural vibration problem [33], the dynamic crack problem [34], the elastodynamic problem [35], the transient heat transfer problem [36] and so on. In this paper, based on the 3D steady potential theory in the literature [21], the theoretical framework of IG-DRBEM for solving the 3D transient heat conduction problem in FGMs will be established.

Solving the normal integral, the nearly singular integral and the singular integral have always been an inevitable research content of BEM. The integral scheme in this paper is adopted similar to the literature [21]. The following is a brief introduction to the integral schemes. For a detailed integral plan, please refer to the literature [21].

In order to accurately calculate the normal integral and simultaneously take into account the computational efficiency, choosing an optimal numerical integration scheme is essential according to the size information of different elements. In 2002, Gao and Davies [37] proposed an adaptive integration method that can automatically select the optimal Gauss integration points to complete the integral calculation. In 2017, Gong and Dong [21] adopted this scheme to compute the normal and nearly singular integral in the 3D steady potential problem. At present, many scholars have proposed many methods [38–40] for solving nearly singular and singular integrals in conventional BEM. But these methods may fail when solving some complex models [41]. In the literature [21], the adaptive integration method was applied successfully to solve the nearly singular integrals in IGBEM. For solving singular integrals, many researchers presented various methods [42–45] to deal with singular integrals in traditional BEM. In 2012, Simpson et al. [1] adopted the self-adaptive coordinate transformation method [42] to solve the

singular integral in IGBEM. In 2017, the power series expansion method was adopted by Gong and Dong to deal with the 3D singular integral in IGBEM for the steady potential problem. These integral schemes in [21] have shown excellent performance, and we expect to still get good numerical results with these schemes in IG-DRBEM for solving 3D transient heat conduction problems in FGMs.

The paper is organized as follows. The governing equation and the definition of the problem are described in Section 2. NURBS basis functions are introduced in Section 3. The deducing process of IG-DRBEM is elaborated in Section 4. In Section 5, the IG-DRBEM postprocessing is presented. In Section 6, three typical numerical examples are discussed in detail for different influencing factors. Finally, the conclusions are summarized in Section 7.

2. Governing equation

In this paper, the transient heat transfer problem of 3D FGMs is considered in a bound domain Ω. The governing equation can be expressed as [46]

$$\frac{\partial}{\partial x_i}\left[k\left(\mathbf{x}\right)\frac{\partial T\left(\mathbf{x},t\right)}{\partial x_i}\right]+g\left(\mathbf{x},t\right)=\rho\left(\mathbf{x}\right)c\left(\mathbf{x}\right)\frac{\partial T\left(\mathbf{x},t\right)}{\partial t},\left(i=1,2,3\right) \tag{1}$$

where $T(\mathbf{x},t)$ and $g(\mathbf{x},t)$ denote the temperature and the heat source at the point $\mathbf{x}=\mathbf{x}(x_1,x_2,x_3)$ and time t. $k(\mathbf{x})$, $\rho(\mathbf{x})$ and $c(\mathbf{x})$ are the thermal conductivity, density and specific heat that vary only with $\mathbf{x}$, respectively.

The temperature and heat flux boundary conditions are considered as follows:

$$T\left(\mathbf{x},t\right)=\overline{T}\left(\mathbf{x},t\right)\ ,\qquad \mathbf{x}\in\Gamma_1 \tag{2}$$

and

$$-k(\mathbf{x})\frac{\partial T}{\partial \mathbf{n}}=\overline{Q}\left(\mathbf{x},t\right)\ ,\qquad \mathbf{x}\in\Gamma_2 \tag{3}$$

where the relations $\Gamma_1\cap\Gamma_2=\varnothing$, $\Gamma_1\cup\Gamma_2=\Gamma$, $\Gamma=\partial\Omega$ need to be satisfied, $\overline{T}$ and $\overline{Q}$ are the known temperature and heat flux functions. $\mathbf{n}$ is the outward normal vector of the boundary Γ. The initial temperature can be given by $T(\mathbf{x},0)=T_0(\mathbf{x})$.

3. NURBS basis functions

In this paper, NURBS basis functions are adopted to describe the geometry and approximate the unknown field variables [21]. A tensor-product NURBS surface can be given by

$$S(\xi,\eta)=\sum_{i=1}^{n}\sum_{j=1}^{m}R_{i,j}^{p,q}(\xi,\eta)P_{i,j} \tag{4}$$

where the bivariate basis functions $R_{i,j}^{p,q}(\xi,\eta)$ can be written as

$$R_{i,j}^{p,q}(\xi,\eta)=\frac{N_{i,p}(\xi)M_{j,q}(\eta)\omega_{i,j}}{\sum_{\hat{i}=1}^{n}\sum_{\hat{j}=1}^{m}N_{\hat{i},p}(\xi)M_{\hat{j},q}(\eta)\omega_{\hat{i},\hat{j}}} \tag{5}$$

in which $N_{i,p}$ and $M_{j,q}$ are respectively the ith B-spline basis function of order p in the direction of ξ and the jth B-spline basis function of order q in the direction of η. $\omega_{i,j}$ is the weight value corresponding to the control point $P_{i,j}$, n and m are the numbers of basis functions at different parametric directions. Here, we define two knot vectors by the non-decreasing sequence of coordinates in the parametric space:

$$\Xi=\left\{\xi_1,\xi_2,\ldots,\xi_{n+p+1}\right\} \tag{6}$$

$$\Pi=\left\{\eta_1,\eta_2,\ldots,\eta_{m+q+1}\right\} \tag{7}$$

The B-spline basis function $N_{i,p}(\xi)$ can be expressed as

$$N_{i,p}(\xi)=\frac{\xi-\xi_i}{\xi_{i+p}-\xi_i}N_{i,p-1}\left(\xi\right)+\frac{\xi_{i+p+1}-\xi}{\xi_{i+p+1}-\xi_{i+1}}N_{i+1,p-1}\left(\xi\right),\qquad p\geq 1 \tag{8}$$

where $1 \leq i \leq n$. Particularly, when $p = 0$, $N_{i,p}$ can be written as

$$N_{i,0} = \begin{cases} 1 & \text{if} \quad \xi_i \leq \xi < \xi_{i+1} \\ 0 & \text{otherwise} \end{cases} \tag{9}$$

A detailed description can be found in the literature [21].

4. Isogeometric dual reciprocity BEM in FGMs

Before introducing the IG-DRBEM, it is necessary to derive the boundary-domain integral equation through the weighted residual method in FGMs. Then the pure boundary integral equation is established by the DRM. Finally, NURBS basis functions are used to discretize the boundary integral, and then the linear equations are formed.

4.1. Boundary-domain integral equation and dual reciprocity process

Similar to traditional BEM, applying the weighted residual method to the governing equation (1) and boundary conditions (2), (3) based on the potential fundamental solution $T^* = 1/(4\pi r(\mathbf{x}', \mathbf{x}))$, the integral equation can be obtained by means of integration by parts. Literature [47] shows the relevant detailed derivation process. The resultant boundary-domain integral equation is shown as follows:

$$\begin{aligned} &C\left(\mathbf{x}'\right)\tilde{T}\left(\mathbf{x}', t\right) + \int_{\Gamma} \tilde{T}\left(\mathbf{x}, t\right) Q^*\left(\mathbf{x}', \mathbf{x}\right) \mathrm{d}\Gamma - \int_{\Gamma} Q\left(\mathbf{x}, t\right) T^*\left(\mathbf{x}', \mathbf{x}\right) \mathrm{d}\Gamma \\ &= \int_{\Omega} T^*\left(\mathbf{x}', \mathbf{x}\right) \left[g\left(\mathbf{x}, t\right) - \frac{\rho\left(\mathbf{x}\right) c\left(\mathbf{x}\right)}{k\left(\mathbf{x}\right)} \frac{\partial \tilde{T}\left(\mathbf{x}, t\right)}{\partial t} + \frac{V\left(\mathbf{x}', \mathbf{x}\right) \tilde{T}\left(\mathbf{x}, t\right)}{T^*\left(\mathbf{x}', \mathbf{x}\right)} \right] \mathrm{d}\Omega \end{aligned} \tag{10}$$

where

$$\begin{cases} \tilde{T}\left(\mathbf{x}, t\right) = k\left(\mathbf{x}\right) T\left(\mathbf{x}, t\right) \\ Q^*(\mathbf{x}', \mathbf{x}) = \partial T^* / \partial \mathbf{n} \\ Q(\mathbf{x}) = k(\mathbf{x}) \partial T / \partial \mathbf{n} \\ V\left(\mathbf{x}', \mathbf{x}\right) = \dfrac{\partial T^*\left(\mathbf{x}', \mathbf{x}\right)}{\partial x_i} \dfrac{\partial \tilde{k}\left(\mathbf{x}\right)}{\partial x_i} \\ \tilde{k}\left(\mathbf{x}\right) = \ln k\left(\mathbf{x}\right) \end{cases} \tag{11}$$

Here, $\tilde{T}$ and $\tilde{k}$ are called the normalized temperature and thermal conductivity. Let

$$\tilde{b}\left(\mathbf{x}, t\right) = \frac{\rho\left(\mathbf{x}\right) c\left(\mathbf{x}\right)}{k\left(\mathbf{x}\right)} \frac{\partial \tilde{T}\left(\mathbf{x}, t\right)}{\partial t} - g\left(\mathbf{x}, t\right) - \frac{V\left(\mathbf{x}', \mathbf{x}\right) \tilde{T}\left(\mathbf{x}, t\right)}{T^*\left(\mathbf{x}', \mathbf{x}\right)} \tag{12}$$

using known basis functions $f_j(r)$, $\tilde{b}$ can be expanded as follows:

$$\tilde{b}\left(\mathbf{x}, t\right) = \sum_{j=1}^{N_t} f_j\left(r\right) \alpha_j\left(t\right) \tag{13}$$

where N_t denotes the total number of points including N_b boundary points and N_I inner points. Generally, $f_j(r)$ is taken to be polynomial form of r such as

$$f_j(\mathbf{x}) = 1 + r_j + r_j^2 + \cdots + r_j^a \tag{14}$$

in which r_j can be expressed as the 2-norm distance, namely $r_j = \left\| \mathbf{x} - \mathbf{x}_j \right\|_2$.

Let $\nabla^2 \hat{T}_j\left(\mathbf{x}\right) = f_j\left(\mathbf{x}\right)$, Eq. (10) can be rewritten as

$$\begin{aligned} &C\left(\mathbf{x}'\right)\tilde{T}\left(\mathbf{x}', t\right) + \int_{\Gamma} \tilde{T}\left(\mathbf{x}, t\right) Q^*\left(\mathbf{x}', \mathbf{x}\right) \mathrm{d}\Gamma - \int_{\Gamma} Q\left(\mathbf{x}, t\right) T^*\left(\mathbf{x}', \mathbf{x}\right) \mathrm{d}\Gamma \\ &= -\sum_{j=1}^{N_t} \alpha_j \int_{\Omega} T^*\left(\mathbf{x}', \mathbf{x}\right) \left(\nabla^2 \hat{T}_j\left(\mathbf{x}\right) \right) \mathrm{d}\Omega \end{aligned} \tag{15}$$

where $\hat{T}_j(\mathbf{x})$ is known when $f_j(\mathbf{x})$ is specified. For example, when $f_j(\mathbf{x})$ is given by Eq. (14), $\hat{T}_j(\mathbf{x})$ can be expressed as

$$\hat{T}_j(\mathbf{x}) = \frac{r_j^2}{6} + \frac{r_j^3}{12} + \cdots + \frac{r_j^{a+2}}{(a+2)(a+3)} \tag{16}$$

Based on this, a pure boundary integral equation can be obtained as follows:

$$\begin{aligned} &C\left(\mathbf{x}'\right)\tilde{T}\left(\mathbf{x}',t\right) + \int_\Gamma \tilde{T}\left(\mathbf{x},t\right) Q^*\left(\mathbf{x}',\mathbf{x}\right) \mathrm{d}\Gamma - \int_\Gamma Q\left(\mathbf{x},t\right) T^*\left(\mathbf{x}',\mathbf{x}\right) \mathrm{d}\Gamma \\ &= \sum_{j=1}^{N_t} \alpha_j \left[C\left(\mathbf{x}'\right)\hat{T}_j\left(\mathbf{x}'\right) + \int_\Gamma \hat{T}_j\left(\mathbf{x}\right) Q^*\left(\mathbf{x}',\mathbf{x}\right) \mathrm{d}\Gamma - \int_\Gamma \hat{Q}_j\left(\mathbf{x}\right) T^*\left(\mathbf{x}',\mathbf{x}\right) \mathrm{d}\Gamma \right] \end{aligned} \tag{17}$$

where $\hat{Q}_j(\mathbf{x}) = \partial \hat{T}_j(\mathbf{x}) / \partial \mathbf{n}$ and $C(\mathbf{x}')$ is a jump term in which it can be obtained similar to the conventional BEM [24]. Considering Eq. (16), $\hat{Q}_j$ can be computed by

$$\hat{Q}_j = \left(r_{jx_1} \frac{\partial x_1}{\partial \mathbf{n}} + r_{jx_2} \frac{\partial x_2}{\partial \mathbf{n}} + r_{jx_3} \frac{\partial x_3}{\partial \mathbf{n}} \right) \left(\frac{1}{3} + \frac{r_j}{4} + \cdots + \frac{r_j^a}{a+3} \right) \tag{18}$$

4.2. NURBS approximation and formation of systems of linear equations

The variables $\mathbf{x}$, $\tilde{T}$, Q, $\hat{T}_v$ and $\hat{Q}_v$ in Eq. (17) can be expressed by NURBS as follows:

$$\begin{cases} \mathbf{x}(\xi,\eta) = \sum_{i=1}^{n}\sum_{j=1}^{m} R_{i,j}^{p,q}(\xi,\eta)\, \mathbf{x}_{ij} \\ \tilde{T}(\xi,\eta) = \sum_{i=1}^{n}\sum_{j=1}^{m} R_{i,j}^{p,q}(\xi,\eta)\, \tilde{T}_{ij} \\ Q(\xi,\eta) = \sum_{i=1}^{n}\sum_{j=1}^{m} R_{i,j}^{p,q}(\xi,\eta)\, Q_{ij} \\ \hat{T}_v(\xi,\eta) = \sum_{i=1}^{n}\sum_{j=1}^{m} R_{i,j}^{p,q}(\xi,\eta)\, \hat{T}_{u_{ij}v} \\ \hat{Q}_v(\xi,\eta) = \sum_{i=1}^{n}\sum_{j=1}^{m} R_{i,j}^{p,q}(\xi,\eta)\, \hat{Q}_{u_{ij}v} \end{cases} \tag{19}$$

where $\mathbf{x}_{ij}$ is the coordinate of control point, $\tilde{T}_{ij}$ and Q_{ij} are the control point coefficients of normalized temperature and heat flux, $\hat{T}_{u_{ij}v}$ and $\hat{Q}_{u_{ij}v}$ represent the control point coefficients corresponding to the function values of the distance from point u to point v. On the left side of Eq. (19), all quantities are the values of the variables at the collocation point with parameter (ξ, η).

To facilitate the numerical integration, the integral interval needs to be transformed as $\hat{\xi}$ or $\hat{\eta} \in [-1, 1]$. Assuming that the eth interval is expressed as $[\xi_e, \xi_{e+1}]$ and $[\eta_e, \eta_{e+1}]$, the relation exists

$$J^e\left(\hat{\xi},\hat{\eta}\right) = \frac{\mathrm{d}\Gamma}{\mathrm{d}\xi \mathrm{d}\eta} \frac{\mathrm{d}\xi \mathrm{d}\eta}{\mathrm{d}\hat{\xi}\mathrm{d}\hat{\eta}} \tag{20}$$

where

$$\frac{\mathrm{d}\Gamma}{\mathrm{d}\xi \mathrm{d}\eta} = \left(\left(x_{2,\xi}x_{3,\eta} - x_{3,\xi}x_{2,\eta}\right)^2 + \left(x_{3,\xi}x_{1,\eta} - x_{1,\xi}x_{3,\eta}\right)^2 + \left(x_{1,\xi}x_{2,\eta} - x_{2,\xi}x_{1,\eta}\right)^2 \right)^{1/2} \tag{21}$$

in which

$$\mathrm{d}\xi \mathrm{d}\eta = \frac{(\xi_{e+1} - \xi_e)(\eta_{e+1} - \eta_e)}{4} \mathrm{d}\hat{\xi}\mathrm{d}\hat{\eta} \tag{22}$$

Note that $x_{u,v}$ denotes $\partial x_u / \partial v$ in Eq. (21). According to the local support property of NURBS basis functions and applying the relation Eq. (20), a set of local basis functions that are related to the global basis functions can be

expressed as

$$N_b^e(\hat{\xi},\hat{\eta}) \equiv R_{i,j}^{p,q}(\xi\left(\hat{\xi}\right),\eta\left(\hat{\eta}\right)) \tag{23}$$

Based on this, Eq. (19) can be rewritten as

$$\begin{cases} \mathbf{x}\left(\hat{\xi},\hat{\eta}\right) = \sum_{b=1}^{(p+1)(q+1)} N_b^e\left(\hat{\xi},\hat{\eta}\right)\mathbf{x}_b \\ \tilde{T}\left(\hat{\xi},\hat{\eta}\right) = \sum_{b=1}^{(p+1)(q+1)} N_b^e\left(\hat{\xi},\hat{\eta}\right)\tilde{T}_b \\ Q\left(\hat{\xi},\hat{\eta}\right) = \sum_{b=1}^{(p+1)(q+1)} N_b^e\left(\hat{\xi},\hat{\eta}\right)Q_b \\ \hat{T}_v\left(\hat{\xi},\hat{\eta}\right) = \sum_{b=1}^{(p+1)(q+1)} N_b^e\left(\hat{\xi},\hat{\eta}\right)\hat{T}_{bv}^e \\ \hat{Q}_v\left(\hat{\xi},\hat{\eta}\right) = \sum_{b=1}^{(p+1)(q+1)} N_b^e\left(\hat{\xi},\hat{\eta}\right)\hat{Q}_{bv}^e \end{cases} \tag{24}$$

Note that Eq. (24) has exactly the same property as the variables in Eq. (19), but Eq. (19) indicates the global variables, while Eq. (24) only indicates the variables in Eq. (19) on a certain boundary element.

Substituting Eq. (24) into Eq. (17), the discrete isogeometric dual reciprocity formulation with FGMs can be obtained as follows:

$$\begin{aligned} &C\left(\mathbf{x}_b\right)\sum_{b=1}^{N_{pq}} N_b^{e'}\left(\hat{\xi}',\hat{\eta}'\right)\tilde{T}_b^{e'} + \sum_{e=1}^{N_e}\sum_{b=1}^{N_{pq}}\left[\int_{-1}^{1}\int_{-1}^{1} Q^*\left(\mathbf{x}_b,\mathbf{x}(\hat{\xi},\hat{\eta})\right)N_b^e(\hat{\xi},\hat{\eta})J^e(\hat{\xi},\hat{\eta})\mathrm{d}\hat{\xi}\mathrm{d}\hat{\eta}\right]\tilde{T}_b^e \\ &-\sum_{e=1}^{N_e}\sum_{b=1}^{N_{pq}}\left[\int_{-1}^{1}\int_{-1}^{1} T^*\left(\mathbf{x}_b,\mathbf{x}(\hat{\xi},\hat{\eta})\right)N_b^e(\hat{\xi},\hat{\eta})J^e(\hat{\xi},\hat{\eta})\mathrm{d}\hat{\xi}\mathrm{d}\hat{\eta}\right]Q_b^e \\ &=\sum_{v=1}^{N_t}\alpha_v\left\{C\left(\mathbf{x}_b\right)\sum_{b=1}^{N_{pq}} N_b^{e'}\left(\hat{\xi}',\hat{\eta}'\right)\hat{T}_{bv}^{e'}\right. \\ &+\sum_{e=1}^{N_e}\sum_{b=1}^{N_{pq}}\left[\int_{-1}^{1}\int_{-1}^{1} Q^*\left(\mathbf{x}_b,\mathbf{x}(\hat{\xi},\hat{\eta})\right)N_b^e(\hat{\xi},\hat{\eta})J^e(\hat{\xi},\hat{\eta})\mathrm{d}\hat{\xi}\mathrm{d}\hat{\eta}\right]\hat{T}_{bv}^e \\ &\left.-\sum_{e=1}^{N_e}\sum_{b=1}^{N_{pq}}\left[\int_{-1}^{1}\int_{-1}^{1} T^*\left(\mathbf{x}_b,\mathbf{x}(\hat{\xi},\hat{\eta})\right)N_b^e(\hat{\xi},\hat{\eta})J^e(\hat{\xi},\hat{\eta})\mathrm{d}\hat{\xi}\mathrm{d}\hat{\eta}\right]\hat{Q}_{bv}^e\right\} \end{aligned} \tag{25}$$

where N_e represents the number of elements, and $N_{pq} = (p+1)(q+1)$, $\mathbf{x}_b \in \Gamma$. To ensure the positions of collocation points on the real boundary, the Greville abscissae method [1] is used to generate the collocation points in parameter space. For example, the collocation point (ξ_i', η_j') in parameter space can be given by

$$\begin{cases} \xi_i' = \dfrac{\xi_{i+1}+\xi_{i+2}+\cdots+\xi_{i+p}}{p} & i = 1,2,\ldots,n \\ \eta_j' = \dfrac{\eta_{j+1}+\eta_{j+2}+\cdots+\eta_{j+q}}{q} & j = 1,2,\ldots,m \end{cases} \tag{26}$$

From Eq. (26), the number of boundary collocation points can be expressed by $n \times m$. Assuming that N_b represents the number of boundary collocation points, namely $N_b = n \times m$. It is worth noting that a few internal points are needed to improve the computational accuracy. When the collocation point is placed in the domain Ω, similar to

Eq. (25), the discrete equations of N_I internal points can be written as

$$\begin{aligned}
&\tilde{T}\left(\mathbf{x}_i\right)+\sum_{e=1}^{N_e}\sum_{b=1}^{N_{pq}}\left[\int_{-1}^{1}\int_{-1}^{1}Q^*\left(\mathbf{x}_i,\mathbf{x}(\hat{\xi},\hat{\eta})\right)N_b^e(\hat{\xi},\hat{\eta})J^e(\hat{\xi},\hat{\eta})\mathrm{d}\hat{\xi}\mathrm{d}\hat{\eta}\right]\tilde{T}_b^e\\
&-\sum_{e=1}^{N_e}\sum_{b=1}^{N_{pq}}\left[\int_{-1}^{1}\int_{-1}^{1}T^*\left(\mathbf{x}_i,\mathbf{x}(\hat{\xi},\hat{\eta})\right)N_b^e(\hat{\xi},\hat{\eta})J^e(\hat{\xi},\hat{\eta})\mathrm{d}\hat{\xi}\mathrm{d}\hat{\eta}\right]Q_b^e\\
&=\sum_{v=1}^{N_t}\alpha_v\left\{\hat{T}_v\left(\mathbf{x}_i\right)+\sum_{e=1}^{N_e}\sum_{b=1}^{N_{pq}}\left[\int_{-1}^{1}\int_{-1}^{1}Q^*\left(\mathbf{x}_i,\mathbf{x}(\hat{\xi},\hat{\eta})\right)N_b^e(\hat{\xi},\hat{\eta})J^e(\hat{\xi},\hat{\eta})\mathrm{d}\hat{\xi}\mathrm{d}\hat{\eta}\right]\hat{T}_{bv}^e\right.\\
&\left.-\sum_{e=1}^{N_e}\sum_{b=1}^{N_{pq}}\left[\int_{-1}^{1}\int_{-1}^{1}T^*\left(\mathbf{x}_i,\mathbf{x}(\hat{\xi},\hat{\eta})\right)N_b^e(\hat{\xi},\hat{\eta})J^e(\hat{\xi},\hat{\eta})\mathrm{d}\hat{\xi}\mathrm{d}\hat{\eta}\right]\hat{Q}_{bv}^e\right\}
\end{aligned}\tag{27}$$

where the points $\mathbf{x}_i \in \Omega (i = 1, 2, \ldots, N_I)$. Based on this system of linear equations in N_t dimensions can be generated as follows:

$$\mathbf{H}\tilde{\mathbf{T}}-\mathbf{G}\mathbf{Q}=\sum_{v=1}^{N_t}\alpha_v\left(\mathbf{H}\hat{\mathbf{T}}_v-\mathbf{G}\hat{\mathbf{Q}}_v\right)\tag{28}$$

where $N_t = N_b + N_I$, the vectors $\tilde{\mathbf{T}}$ and $\mathbf{Q}$ can be expressed as

$$\begin{cases}\tilde{\mathbf{T}}=[\tilde{T}_1,\tilde{T}_2,\ \cdots,\tilde{T}_{N_b},\tilde{T}_{N_b+1},\ \cdots,\ \tilde{T}_{N_t}]^{\mathrm{T}}\\ \mathbf{Q}=[Q_1,Q_2,\ldots,Q_{N_b}]^{\mathrm{T}}\end{cases}\tag{29}$$

in which the first N_b elements are the normalized temperature coefficients of control points and the last N_I elements are the real normalized temperature of collocation points in the vector $\tilde{\mathbf{T}}$, the vector $\mathbf{Q}$ includes N_b heat flux coefficients of control points, the superscript "T" denotes the transpose of the vector.

The vectors $\hat{\mathbf{T}}_v$ in Eq. (28) are given by

$$\hat{\mathbf{T}}_v=\left[\hat{T}_{1v}\ ,\ \hat{T}_{2v},\ \cdots\ ,\ \hat{T}_{N_bv}\ ,\ \hat{T}_{(N_b+1)v},\ \cdots\ ,\hat{T}_{N_tv}\right]^{\mathrm{T}}\tag{30}$$

where $\hat{T}_{lv}=\hat{T}_v(\mathbf{x}_l), (l = 1, 2, \ldots, N_t)$, $\{\mathbf{x}_l\}_{l=1}^{N_t}$ denote the full set of points including boundary and interior points. The vectors $\hat{\mathbf{Q}}_v$ are written as

$$\hat{\mathbf{Q}}_v=\left[\hat{Q}_{1v},\ \ \hat{Q}_{2v}\ ,\ \cdots\ ,\ \hat{Q}_{N_bv}\right]^{\mathrm{T}}\tag{31}$$

where $\hat{Q}_{lv}=\hat{Q}_v(\mathbf{x}_l), (l = 1, 2, \ldots, N_b)$. Similar to Eq. (29), the first N_b elements in vector $\hat{\mathbf{T}}_v$ and all elements of vector $\hat{\mathbf{Q}}_v$ denote the control point coefficients corresponding to the function values of the distance between the boundary collocation points and point v. The last N_I elements in vector $\hat{\mathbf{T}}_v$ indicate the function values of the distance from the interior points to point v.

Here, the matrices $\hat{\mathbf{T}}$ ($\hat{\mathbf{T}} \in \mathrm{R}^{N_t\times N_t}$) and $\hat{\mathbf{Q}}$ ($\hat{\mathbf{Q}} \in \mathrm{R}^{N_b\times N_t}$) containing of vectors $\hat{\mathbf{T}}_v$ and $\hat{\mathbf{Q}}_v$ (as columns) are introduced, and time-dependent vector $\boldsymbol{\alpha}=\boldsymbol{\alpha}(t)$ ($\boldsymbol{\alpha} \in \mathrm{R}^{N_t\times 1}$) is used to rewrite Eq. (13), applying at N_t points, i.e.

$$\boldsymbol{\alpha}=\mathbf{F}^{-1}\tilde{\mathbf{b}}\tag{32}$$

where $\mathbf{F} \in \mathrm{R}^{N_t\times N_t}$, $\tilde{\mathbf{b}}=\tilde{\mathbf{b}}(t) \in \mathrm{R}^{N_t\times 1}$. Elements of the matrix $\mathbf{F}$ are formed by

$$F_{lj}=f_j(\mathbf{x}_l), (l = 1, 2, \ldots, N_t)\tag{33}$$

where the function f_j is given by Eq. (14). For any source point $\mathbf{x}_j$, the element of the vector $\tilde{\mathbf{b}}$ for any field point $\mathbf{x}_i$ can be generated by

$$b_i\left(\mathbf{x}_i,t\right)=\frac{\rho\left(\mathbf{x}_i\right)c\left(\mathbf{x}_i\right)}{k\left(\mathbf{x}_i\right)}\frac{\partial\tilde{T}\left(\mathbf{x}_i,t\right)}{\partial t}-g\left(\mathbf{x}_i,t\right)-\frac{V\left(\mathbf{x}_j,\mathbf{x}_i\right)\tilde{T}\left(\mathbf{x}_i,t\right)}{T^*\left(\mathbf{x}_j,\mathbf{x}_i\right)}\tag{34}$$

Eq. (28) can be rewritten as

$$\mathbf{H}\tilde{\mathbf{T}}-\mathbf{G}\mathbf{Q}=\left(\mathbf{H}\hat{\mathbf{T}}-\mathbf{G}\hat{\mathbf{q}}\right)\mathbf{F}^{-1}\tilde{\mathbf{b}}\tag{35}$$

Let $\mathbf{C} = -\left(\mathbf{H}\hat{\mathbf{T}} - \mathbf{G}\hat{\mathbf{q}}\right)\mathbf{F}^{-1}$, Eq. (35) can be expressed as

$$\mathbf{C}\tilde{\mathbf{b}} + \mathbf{H}\tilde{\mathbf{T}} = \mathbf{G}\mathbf{Q} \tag{36}$$

Let $K_i(\mathbf{x}_i) = (\rho(\mathbf{x}_i)\, c(\mathbf{x}_i))/k(\mathbf{x}_i)$, the vector $\mathbf{K}$ can be obtained by applying N_t collocation points as follows:

$$\mathbf{K} = \left[K_1, K_2, K_3, \ldots, \quad K_{N_t}\right]^{\mathrm{T}} \tag{37}$$

To describe conveniently, the matrices $\mathbf{E}$, $\mathbf{A}$, $\mathbf{D}$, and $\mathbf{R}$ need to be introduced in the following formulation. The elements in matrix $\mathbf{E}$ are defined by $E_{ij} = C_{ij}K_j$, $(i, j = 1, 2, \ldots, N_t)$. Let $A_{ij} = V\left(\mathbf{x}_j, \mathbf{x}_i\right)/T^*\left(\mathbf{x}_j, \mathbf{x}_i\right)$, $(i, j = 1, 2, \ldots, N_t)$, the detailed expression of the elements in matrix $\mathbf{A}$ can be written as

$$A_{ij} = \frac{1}{k(\mathbf{x}_i)\, r^2\left(\mathbf{x}_i, \mathbf{x}_j\right)} \sum_{l=1}^{3} \frac{\partial k(\mathbf{x}_i)}{\partial x_{il}}(x_{jl} - x_{il}) \tag{38}$$

where x_{jl} denotes the lth direction coordinate of the point $\mathbf{x}_j(x_{j1}, x_{j2}, x_{j3})$. The elements in matrix $\mathbf{D}$ are written as $D_{ij} = C_{ij}A_{ji}$, $(i, j = 1, 2, \ldots, N_t)$. The structure of matrix $\mathbf{R}$ can be represented as follows:

$$\mathbf{R} = \begin{bmatrix} (\mathbf{R}_{\Delta})_{N_b \times N_b} & \mathbf{0}_{N_b \times N_I} \\ \mathbf{0}_{N_I \times N_b} & (\mathbf{I})_{N_I \times N_I} \end{bmatrix} \tag{39}$$

where the elements in $\mathbf{R}_{\Delta}$ are generated by NURBS basis functions $R_{i,j}^{p,q}(\xi, \eta)$. For instance, if $(\mathbf{R}_{\Delta})_{\tilde{n}\tilde{m}}$ is the element of $\mathbf{R}_{\Delta}$ in row $\tilde{n}$ and column $\tilde{m}$, then $(\mathbf{R}_{\Delta})_{\tilde{n}\tilde{m}}$ can be defined as the function value of the $\tilde{m}$-th NURBS basis function substituted by the parameter value (ξ, η) of the $\tilde{n}$-th boundary collocation point in the knot vector space. In addition, note that the derivation term $\partial T/\partial t$ in Eq. (34) is replaced generally by the time difference. Considering matrices $\mathbf{E}$, $\mathbf{A}$, $\mathbf{D}$, and $\mathbf{R}$, Eq. (36) can be rewritten as

$$\mathbf{E}\mathbf{R}\frac{\partial \tilde{\mathbf{T}}(t)}{\partial t} + (\mathbf{H} - \mathbf{D}\mathbf{R})\tilde{\mathbf{T}}(t) = \mathbf{G}\mathbf{Q}(t) + \mathbf{C}\mathbf{g}(t) \tag{40}$$

It can be seen from Eq. (38) that the values of elements have infinite cases when $r = 0$. To compute elements accurately in $\mathbf{D}$, similar to the rigid body displacement method in traditional BEM, the element D_{ij} $(i = j)$ can be computed indirectly. Because the elements in $\mathbf{D}$ are independent of the temperature and heat source only with geometry information and thermal conductivity. Based on this, assuming that the temperature field is uniform and the value equals the unit without the heat source, then Eq. (40) can be written as

$$\mathbf{D}\mathbf{R}\tilde{\mathbf{T}} = \mathbf{H}\tilde{\mathbf{T}} \tag{41}$$

When the matrix $\mathbf{H}$ and the asymmetric elements in matrix $\mathbf{D}$ are obtained, applying Eq. (41) the elements D_{ii} $(i = 1, 2, \ldots, N_t)$ can be computed as follows:

$$D_{ii} = \left(\sum_{j=1}^{N_t} H_{ij}\tilde{T}_j - \sum_{\substack{j=1 \\ j \neq i}}^{N_t} D_{ij} \sum_{m=1}^{N_t} R_{jm}\tilde{T}_m\right) \Bigg/ \sum_{m=1}^{N_t} R_{im}\tilde{T}_m \tag{42}$$

The unknown $\tilde{T}$ and Q are obtained by solving Eq. (40). Further, the normalized temperature and the heat flux of collocation points on the boundary can be given by Eq. (24). Finally, the real temperature of collocation point T can be solved by $T(\mathbf{x}, t) = \tilde{T}(\mathbf{x}, t)/k(\mathbf{x})$.

4.3. Two-level time integration

Assume that $\tilde{\mathbf{T}}$, $\mathbf{Q}$ and $\mathbf{g}$ can be approximated by a linear combination of values at moments t_s and t_{s+1}, where $\Delta t = t_{s+1} - t_s$ denotes the time step size. $\tilde{\mathbf{T}}$, $\mathbf{Q}$ and $\mathbf{g}$ in Eq. (40) can be written as

$$\begin{cases} \tilde{T} = (1 - \theta_T)\,\tilde{T}^s + \theta_T \tilde{T}^{s+1} \\ Q = \left(1 - \theta_Q\right) Q^s + \theta_Q Q^{s+1} \\ g = \left(1 - \theta_g\right) g^s + \theta_g g^{s+1} \end{cases} \tag{43}$$

where θ_T, θ_Q, and θ_g ($\in [0,1]$) are relaxation factors. In addition, the derivation term $\partial\tilde{T}/\partial t$ is replaced by $\left(\tilde{T}^{s+1}-\tilde{T}^{s}\right)/\Delta t$.

Substituting Eq. (43) into Eq. (40), for any time interval $[t_s, t_{s+1}]$, the linear system of equations can be given by

$$\begin{aligned}&\left[\frac{\mathbf{ER}}{\Delta t}+\theta_T\left(\mathbf{H}-\mathbf{DR}\right)\right]\tilde{\mathbf{T}}^{s+1}-\theta_Q\mathbf{GQ}^{s+1}\\&=\left[\frac{\mathbf{ER}}{\Delta t}-\left(1-\theta_T\right)\left(\mathbf{H}-\mathbf{DR}\right)\right]\tilde{\mathbf{T}}^{s}+\left(1-\theta_Q\right)\mathbf{GQ}^{s}+\mathbf{C}\left[\left(1-\theta_g\right)\mathbf{g}^{s}+\theta_g\mathbf{g}^{s+1}\right]\end{aligned}\tag{44}$$

where the superscript "s" denotes the moment t_s. Applying the initial condition T_0 and the known boundary condition T or Q to Eq. (44), the unknown temperature in the domain and the unknown heat flux on the boundary can be solved step by step. In order to realize the automatic starting calculation of Eq. (44) with only the initial temperature condition T_0 besides the boundary condition, θ_T, θ_Q, and θ_g are set to 1 at the first time step, and the appropriate values of the relaxation factors at the other time steps will be discussed in Section 6.1 (B).

5. IG-DRBEM postprocessing

Generally, only a few control points are needed to accurately describe the geometry when NURBS is used. In this case, the element size is usually larger. However, in many cases, the response at any point in the geometry is also urgently needed. Therefore, how to compute quickly the temperature at any point within the element or domain is very important in terms of whether the overall temperature distribution can be directly reflected. When the unknown coefficients of control points and the temperature of interior points are obtained, any point temperature in the element can be interpolated by the second formulation in Eq. (24). For any point in the internal domain, the temperature can be calculated by Eq. (27).

The detailed flowchart is shown in Fig. 1.

All control point coefficients are calculated by NURBS basis function matrix $\mathbf{R}$. In the flowchart, CP, NCIP, and ABIP respectively represent collocation points, new computational interior points (as shown in Section 6.2), and added boundary-element interpolation point (as shown in Section 6.3).

6. Numerical examples

To verify the performance of the proposed method, three different types of errors such as the absolute error (Abserr), the relative error (Relerr), and the relative L_2 error norm (e_{L_2}) are adopted, where e_{L_2} is used to evaluate the overall error. These errors can be respectively expressed as

$$\begin{cases}Abserr=\left|T_{cal}-T_{ref}\right|\\Relerr=100\cdot\left|T_{cal}-T_{ref}\right|\,/\,\left|T_{ref}\right|\\e_{L_2}=\left\|\mathbf{T}_{ref}-\mathbf{T}_{cal}\right\|_{L_2}\,/\,\left\|\mathbf{T}_{ref}\right\|_{L_2}\end{cases}\tag{45}$$

where the L_2 norm $\left\|\mathbf{T}_{ref}\right\|_{L_2}$ can be written as

$$\left\|\mathbf{T}_{ref}\right\|_{L_2}=\sqrt{\sum_{i=1}^{N_t}T_{ref,i}^2}\tag{46}$$

The subscripts "*cal*" and "*ref*" in the above description denote the calculated result and the reference solution. In the sketch figures of the following examples, the green ball and the solid line represent the control point and the NURBS element, respectively.

6.1. A torus model with temperature boundary conditions

In this example, a torus with an outside diameter of 1 and an inside diameter of 0.5 is considered, where the thermal conductivity $k(\mathbf{x})=\cos(x_1)\cos(x_2)\cos(x_3)$, the density ρ and the specify heat c are set to 1. The temperature field is assumed as $T_{exact}=e^{x_1+t}+e^{x_2+t}+e^{x_3+t}$. The initial condition and the temperature boundary condition are

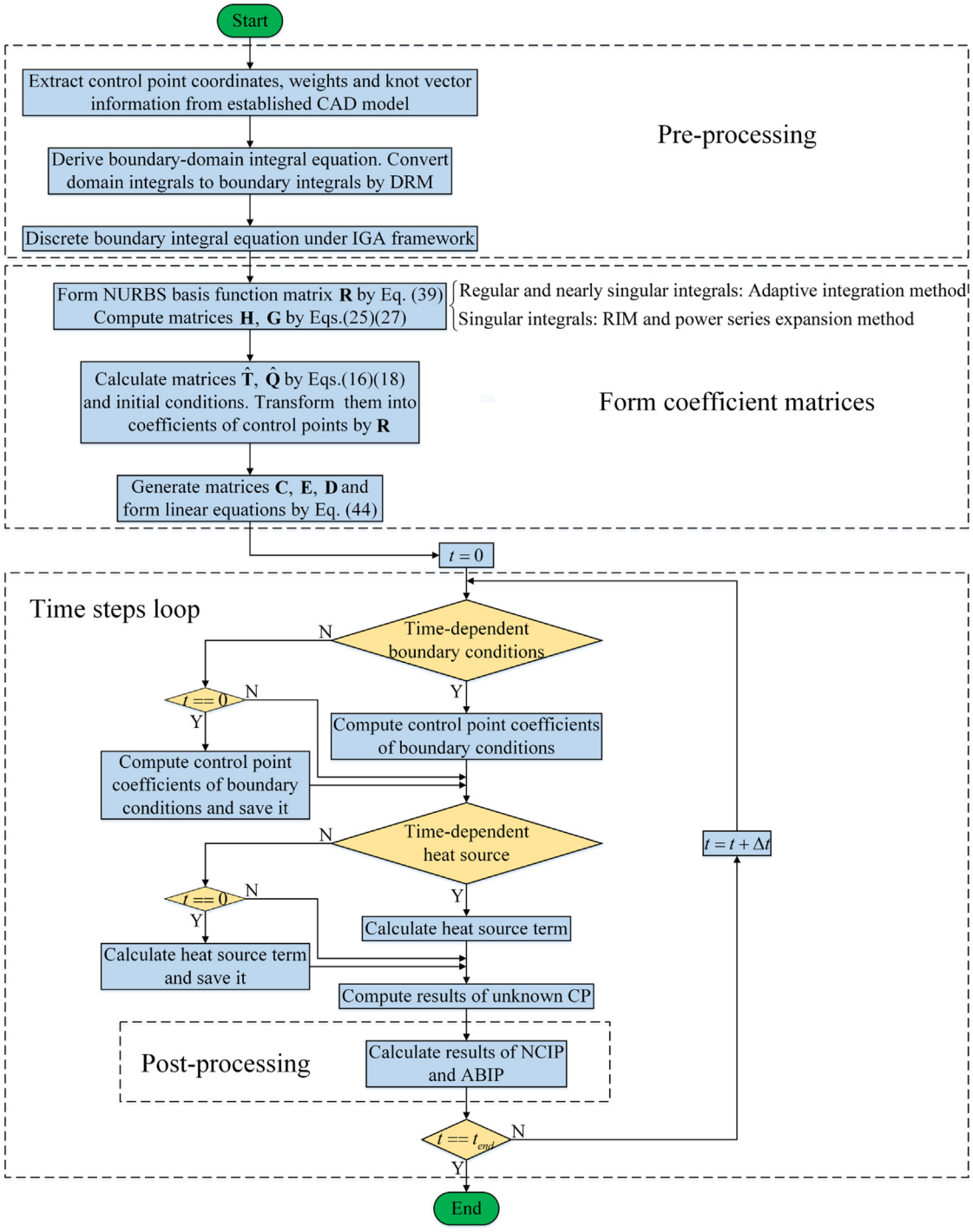

Fig. 1. Flowchart of IG-DRBEM for solving transient heat transfer problems in FGMs.

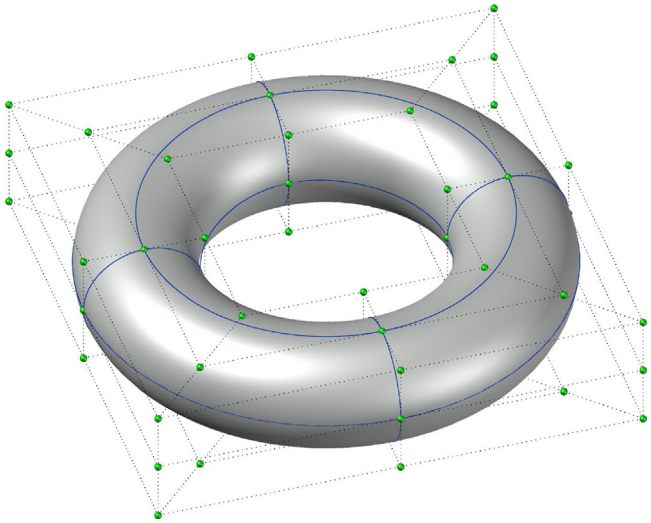

Fig. 2. The torus computation model.

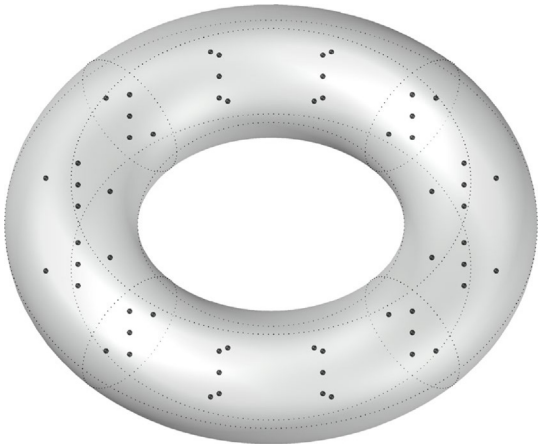

Fig. 3. The distribution of 60 interior points.

specified by the exact expression T_{exact}. Based on the governing equation Eq. (1), the heat source function $g(\mathbf{x}, t)$ can be given by

$$\begin{aligned} g = & \left(1+\sin(x_1)\cos(x_2)\cos(x_3)\right) e^{x_1+t} \\ & + \left(1+\sin(x_2)\cos(x_1)\cos(x_3)\right) e^{x_2+t} \\ & + \left(1+\sin(x_3)\cos(x_2)\cos(x_1)\right) e^{x_3+t} \\ & - \cos(x_1)\cos(x_2)\cos(x_3)\left(e^{x_1+t}+e^{x_2+t}+e^{x_3+t}\right) \end{aligned} \tag{47}$$

As shown in Fig. 2, 16 elements with 81 control points are used, where the knot vectors are shown in Table 1. 124 collocation points which include 64 boundary collocation points and 60 interior points, are used in the computation process. 60 interior points are uniformly distributed into the domain as shown in Fig. 3. In this example, the approximation function f_j, the time step, the number of interior points, the minimum distance from the interior point to the boundary and the different refinements are considered.

Table 1
The knot vector information of the torus model with $p = q = 2$.

Direction	Knot vector
ξ	{0, 0, 0, 1, 1, 2, 2, 3, 3, 4, 4, 4}
η	{0, 0, 0, 1, 1, 2, 2, 3, 3, 4, 4, 4}

Table 2
Results with different expansions of f_j at $t = 1$.

f_j	Mabserr	Mrelerr(%)	e_{L_2}
(i)	0.0499	0.4328	1.3388e−03
(ii)	0.0906	0.7572	2.1815e−03

Table 3
Results adopting different time difference schemes at $t = 1$.

Time difference scheme	Mabserr	Mrelerr(%)	e_{L_2}
Central difference	0.0499	0.4328	1.3388e−03
Galerkin	0.0502	0.4356	1.3453e−03
Backward difference	0.0508	0.4411	1.3590e−03

(A) The effect of different approximation functions f_j

In this case, the two approximation functions are considered as follows:

(i). $f_j = 1 + r_j$
(ii). $f_j = 1 + r_j + r_j^2$

The time step $\Delta t = 0.01$ is used, the relaxation factors θ_T, θ_Q, θ_g are set to 1 at the first time step and 0.5 at the remaining time steps.

It can be seen from Table 2 that the results calculated using (i) are more accurate than (ii) from the perspectives of the maximum absolute error (Mabserr), maximum relative error, and e_{L_2}. Based on this, $f_j = 1 + r_j$ is adopted in the following examples.

(B) The influence of different time difference schemes

Compared with case (A), in order to discuss the effect of different relaxation factors on the numerical results, only the time difference scheme is changed in this case. θ_T, θ_Q and θ_g are still set to 1 for the first time step, and 0.5, 2/3 and 1 for other time steps respectively correspond to the central difference scheme, Galerkin scheme and backward difference scheme.

It can be seen from Table 3 that although different relaxation factors have no obvious effect on the numerical results, relatively speaking, using the central difference scheme can obtain the best accuracy. Therefore, the central difference scheme will be adopted in all subsequent examples.

(C) The effect of time steps

In this case, the same boundary conditions and physical parameters are used as in case (A), where $f_j = 1 + r_j$. As shown in Table 4, the accuracy is slightly improved with the decrease of the time step but tends to be stable. Therefore, the accumulation of errors in the presented method is not obvious, and the time step is set to $\Delta t = 0.001$ in the remaining cases of this example.

(D) The effect of the number of interior points

As shown in Fig. 4, the different number of interior points are adopted such as $N_I = 36$, 60, 84 and 108.

It can be seen from Table 5 that when the number of internal points is greater than 36, the e_{L_2} fluctuates slightly, but basically stays at the 10^{-3} magnitude. Therefore, when IG-DRBEM is used to solve the transient heat transfer problem, only a few interior points are needed.

Table 4
Results using different time steps at $t = 1$.

Δt	Mabserr	Mrelerr(%)	e_{L_2}
0.2	0.05270	0.45077	1.40101e−03
0.1	0.05004	0.43493	1.34377e−03
0.05	0.04991	0.43321	1.33979e−03
0.02	0.04988	0.43291	1.33892e−03
0.01	0.04987	0.43287	1.33882e−03
0.001	0.04986	0.43286	1.33879e−03

Table 5
e_{L_2} using different number of interior points at $t = 1$.

N_I	36	60	84	108
e_{L_2}	1.6401e−03	1.3388e−03	1.3821e−03	1.4757e−03

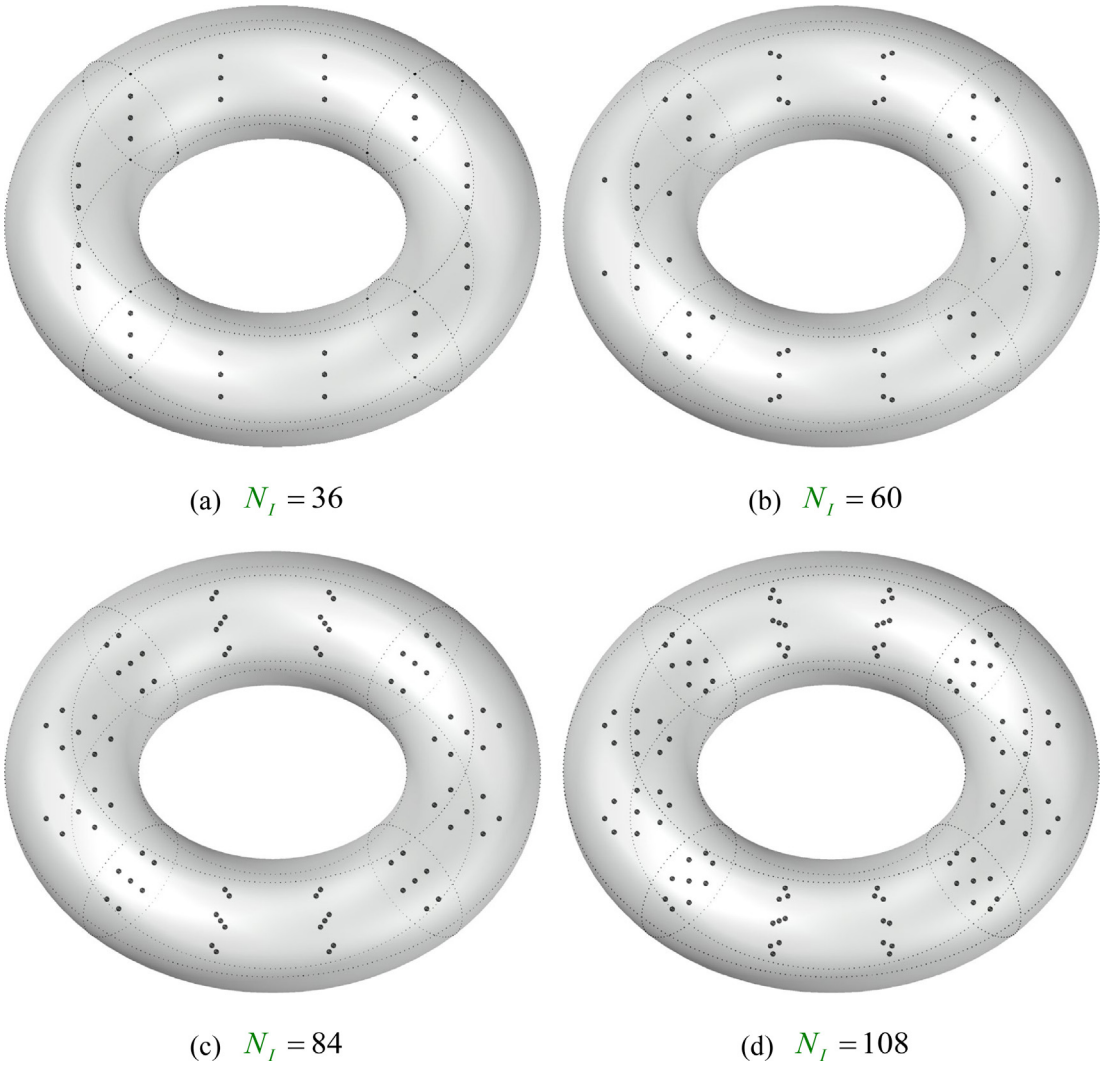

Fig. 4. The torus model with different number of interior points.

Table 6
Temperatures with different δ_{md} at $t = 1$.

Coordinate of new interior point	δ_{md}	IG-DRBEM	Exact	Relerr(%)
(0.9, 0, 0)	0.1	12.1874	12.1224	0.5354
(0.99, 0, 0)	0.01	12.7813	12.7521	0.2290
(0.999, 0, 0)	0.001	12.8243	12.8182	0.0478
(0, 0.9, 0)	0.1	12.1874	12.1224	0.5354
(0, 0.99, 0)	0.01	12.7813	12.7521	0.2290
(0, 0.999, 0)	0.001	12.8243	12.8182	0.0478
(0.75, 0, 0.15)	0.1	11.6455	11.6311	0.1246
(0.75, 0, 0.24)	0.01	11.9273	11.9284	0.0099
(0.75, 0, 0.249)	0.001	11.9593	11.9597	0.0033

Table 7
e_{L_2} with different cases of refinement at $t = 0.1$.

Ref	IG-DRBEM			BEM		
	N_e	N_t	e_{L_2}	N_e	N_t	e_{L_2}
0	16	124	1.33e−03	128	444	9.69e−03
1	64	204	5.40e−04	256	828	7.14e−03
2	144	316	3.85e−04	384	1212	6.53e−03
3	256	460	2.77e−04	768	2364	4.68e−03

(E) The effect of the minimum distance between the interior point and the boundary

In order to show the performance of the proposed method when dealing with nearly singular integrals, the different levels of approach to the boundary (δ_{md}) in a domain are discussed in this case. Adopting the computational model such as Fig. 4(b), the results of some new interior points are shown in Table 6. As δ_{md} gets smaller, the relative error does not increase. Therefore, the present method has a good ability to deal with nearly singular integrals.

(F) The effect of different refinement schemes

In this case, four different element refinement (Ref) schemes for the proposed method and conventional radial integration BEM [47] are discussed as shown respectively in Fig. 5 and Fig. 6, where the interior points in Fig. 4(b) are used in solving process. The e_{L_2} of the two methods under different degrees of freedom are shown in Fig. 7 for comparison.

It can be seen from Table 7 and Fig. 7 that both IG-DRBEM and conventional radial integration BEM converge with the increase of degrees of freedom. But even in the sparsest case with only 16 elements, IG-DRBEM still get accurate results. Besides, according to the literature [31], the radial integration method can accurately represent the domain integral transformation of the known function (such as the heat source term) without approximation. However, the convergence rate of BEM as shown in Fig. 7 is slower than IG-DRBEM. The above two points respectively reflect that IG-DRBEM can obtain higher precision with less calculated cost.

6.2. A gear model with mixed boundary conditions

In this example, a gear model is considered with the mixed boundary conditions. As shown in Fig. 8, the gear is constructed by 981 control points and 216 elements. The knot vector information is shown in Table 8.

The geometry size and the distribution of interior points in the domain of the gear are shown in Fig. 9, where 972 collocation points including 864 boundary collocation points and 108 interior points are considered in the solving process. The 108 interior points are distributed on three different surfaces $x_3 = -0.1, 0, 0.1$, among which four circles with different radius (such as $\delta_r = 0.47, 0.59, 0.71, 0.83$) are distributed on each surface, and 9 interior points are distributed on each circle, namely $9 \times 4 \times 3 = 108$.

Assuming that the exact temperature field is given by

$$T = \cos(x_1)\cos(x_2)\cos(x_3)e^t \tag{48}$$

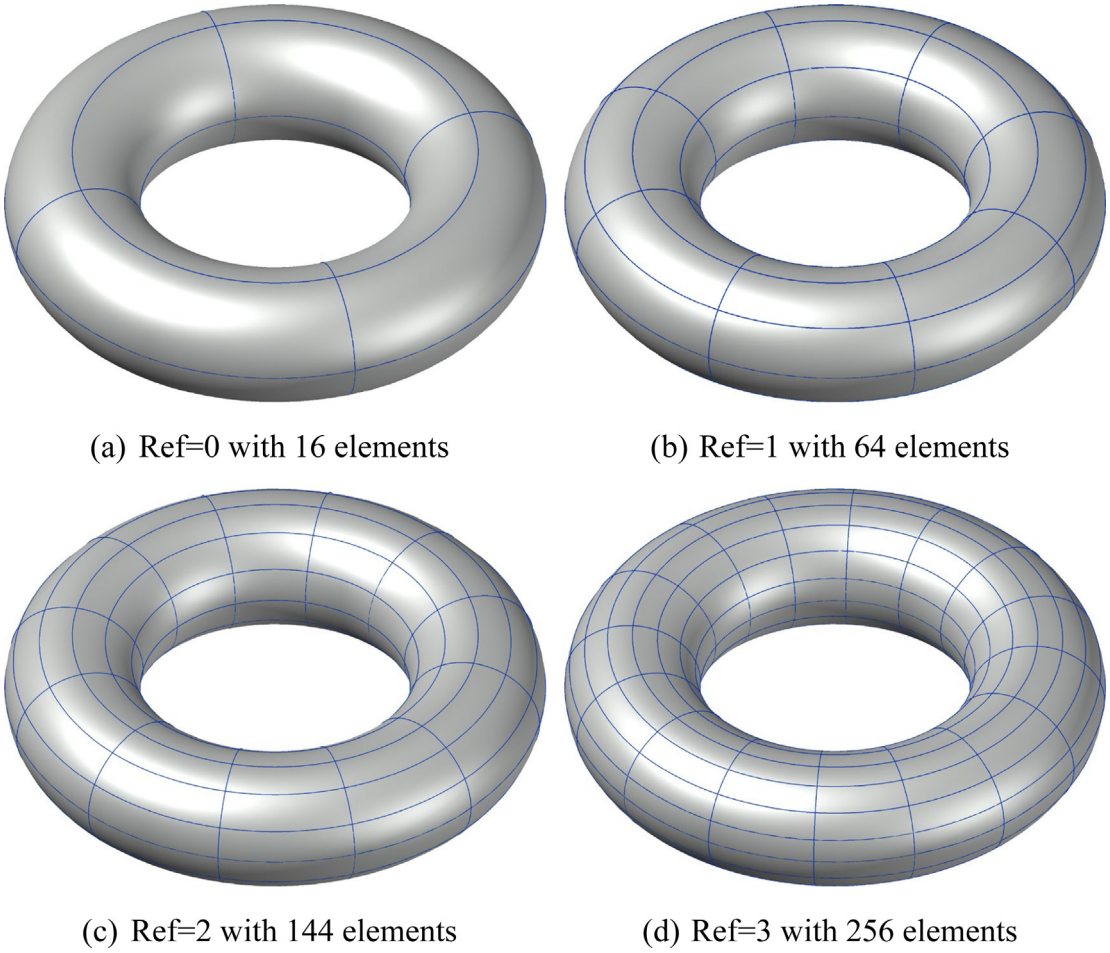

Fig. 5. Different element divisions of torus model for IG-DRBEM.

Table 8
The knot vector information of gear model.

Direction	Order	Knot vector
ξ	$p = 2$	{0, 0, 0, 1, 1, 2, 2, 3, 3, 4, 4, 4, 5, 5, 6, 6, 7, 7, 8, 8, 9, 9, 10, 10, 11, 11, 12, 12, 13, 13, 14, 14, 15, 15, 16, 16, 17, 17, 18, 18, 19, 19, 20, 20, 21, 21, 22, 22, 23, 23, 24, 24, 25, 25, 26, 26, 27, 27, 28, 28, 29, 29, 30, 30, 31, 31, 32, 32, 33, 33, 34, 34, 35, 35, 36, 36, 37, 37, 38, 38, 39, 39, 40, 40, 41, 41, 42, 42, 43, 43, 44, 44, 45, 45, 46, 46, 47, 47, 48, 48, 49, 49, 50, 50, 51, 51, 52, 52, 53, 53, 54, 54, 54}
η	$q = 2$	{0, 0, 0, 1, 1, 2, 2, 3, 3, 4, 4, 4}

the heat conductivity is $k = x_1^2 + x_2^2 + 1$ and the density ρ and the specific heat capacity c are set to 1.0; and subsequently, the heat source g can be written as

$$\begin{aligned} g = e^t \left\{ \left[1 + 3\left(x_1^2 + x_2^2 + 1\right) \right] \cos(x_1)\cos(x_2)\cos(x_3) \right. \\ \left. + 2\left[x_1 \sin(x_1)\cos(x_2)\cos(x_3) + x_2 \sin(x_2)\cos(x_1)\cos(x_3) \right] \right\} \end{aligned} \tag{49}$$

to satisfy the exact solution. Furthermore, the temperature and heat flux boundary conditions are given by means of the exact solution Eq. (48), where the heat flux boundary conditions are applied on the surface of the central hole and the temperature boundary conditions are applied on the remaining parts. In the subsequent analysis, the time

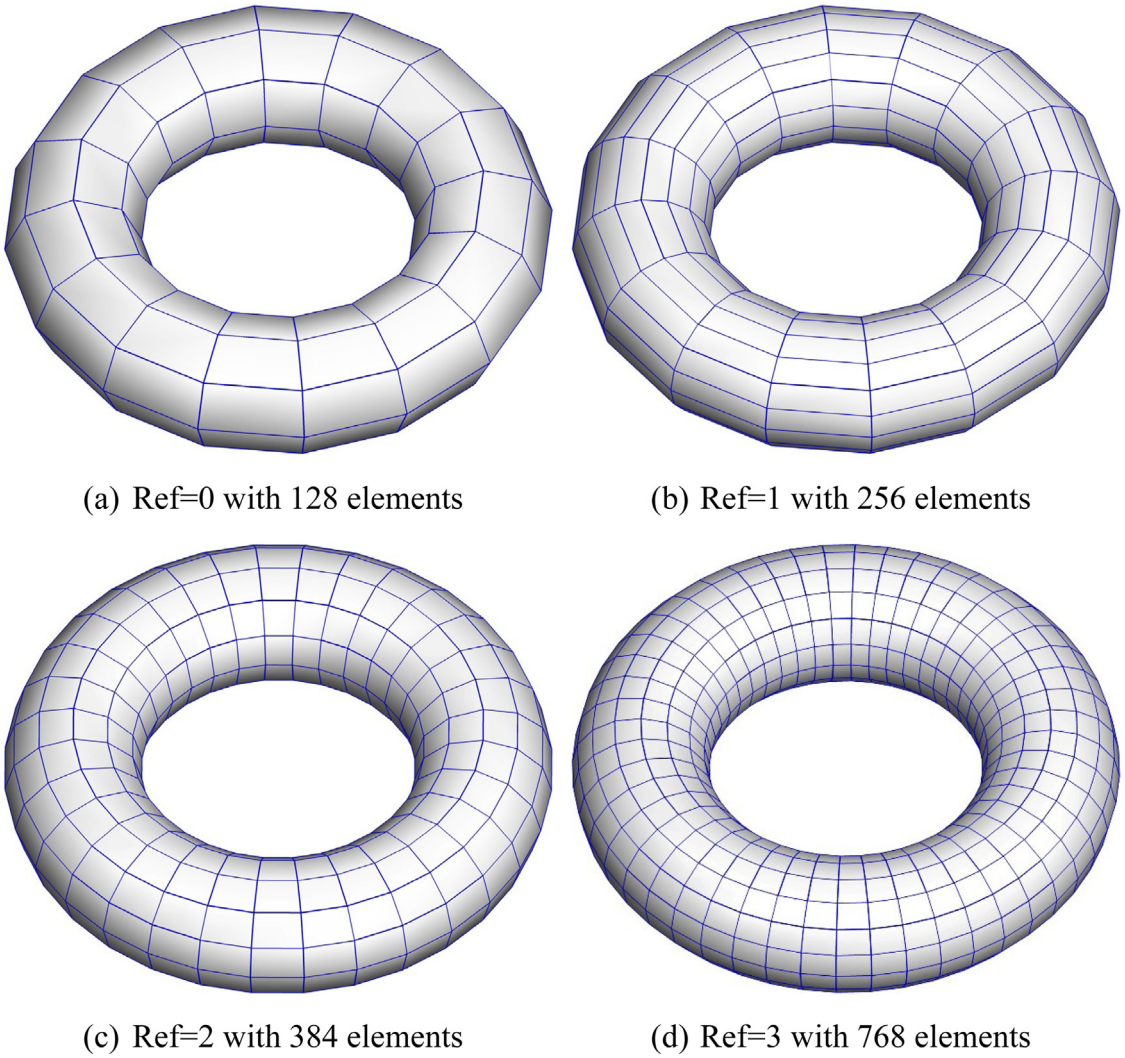

Fig. 6. Different element divisions of torus model for conventional BEM.

step Δt is set as 0.01. The time interval [0, 1] is discussed. The results show that the e_{L_2} is $7.3723e-04$ when $t = 1$.

In order to demonstrate the performance of calculating the temperature of any interior point, Fig. 10 shows the relative errors of using 104 interior points and the relative errors of four temperatures of any interior point obtained based on the computational model of 104 interior points. It can be seen that the Relerrs of the temperature of the four newly computational interior points (NCIP) (Points A, B, C, D in Fig. 9) are acceptable, where the maximum Relerr does not exceed 0.65%. Furthermore, the Relerrs show that the computational results are very stable in different moments such as $t = 0.25$, 0.5, 0.75, and 1.0.

6.3. A multiply connected aircraft model with mixed boundary conditions

In this example, a simple model of aircraft with a cylindrical cavity is considered as shown in Fig. 11. The knot vector information is shown in Table 9. Assuming that the exact temperature field is given by

$$T = 10\left(x_1 + \cos\left(x_2\right) + \mathrm{e}^{x_3}\right)\cos\left(5t\right) \tag{50}$$

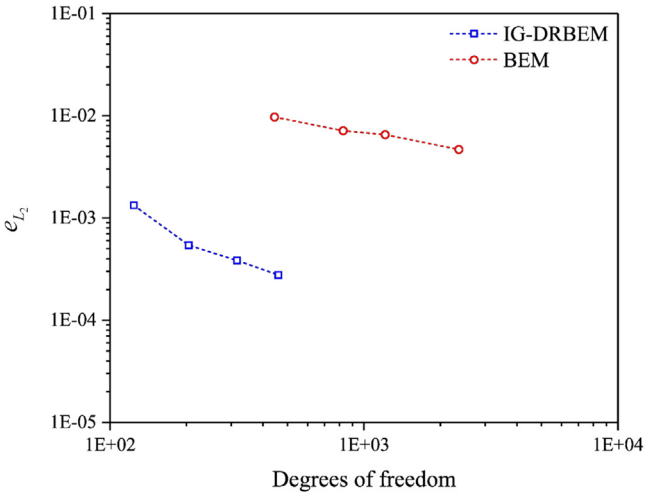

Fig. 7. e_{L_2} using different methods at $t = 0.1$..

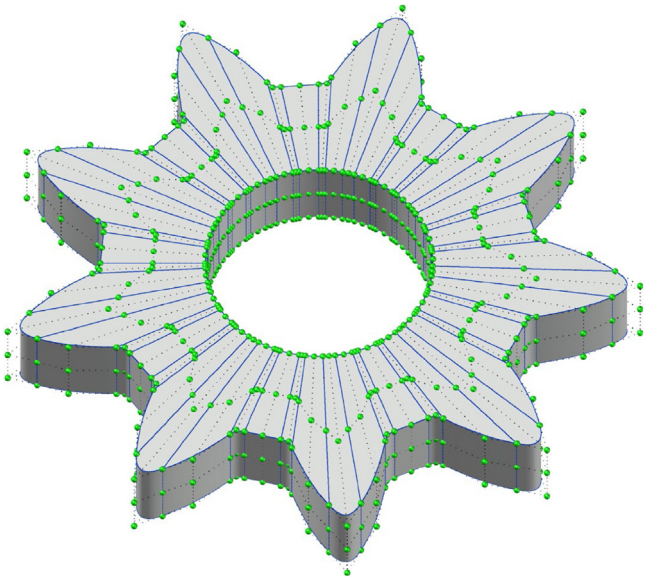

Fig. 8. The computational model of gear with 981 control points and 216 NURBS elements.

the heat source function and the physical property parameter can be expressed as

$$\begin{cases} g = 10e^{x_2^2+x_3^2}\cos(5t)\left[\cos(x_2) - \mathrm{e}^{x_3} + 2\left(x_2\sin(x_2) - x_3\mathrm{e}^{x_3}\right)\right] \\ \qquad\qquad -50\sin(5t)\left(x + \cos(x_2) + \mathrm{e}^{x_3}\right) \\ k = e^{x_2^2+x_3^2}; \quad \rho = \sin^2(x_1); \quad c = \sin(x_1x_2x_3) \end{cases} \tag{51}$$

As shown in Fig. 12, the mixed boundary conditions are considered in this example, where the temperature and heat flux boundary conditions are given by Eq. (50). In this computational model, the inner and outer boundaries are respectively distributed into 1209 and 63 control points, 1104 and 42 boundary collocation points, and 340 and 12 boundary elements, among which 164 interior points are placed in the domain.

To show the temperature field distribution of the aircraft surface, based on the results of the collocation points in Fig. 13(a), the temperature results of ABIP in Fig. 13(b) can be obtained by NURBS interpolation in Eq. (24).

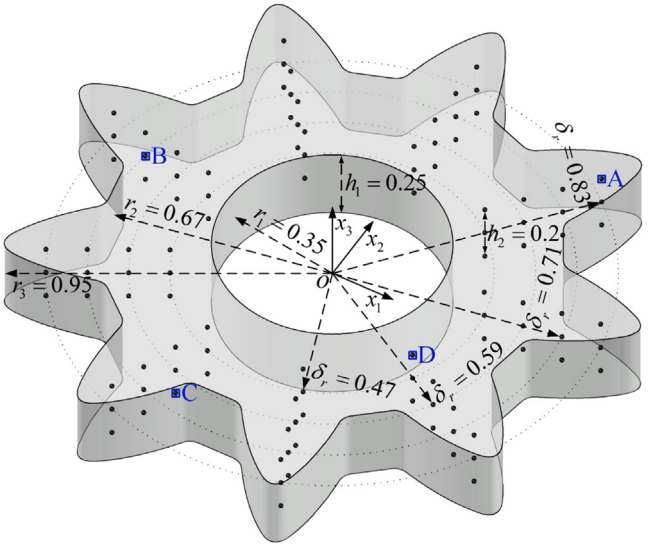

Fig. 9. Geometry description and interior points distribution. r_1: the inside diameter of the gear; r_2: the radius of root circle; r_3: the radius of outside circle; h: the gear thickness.

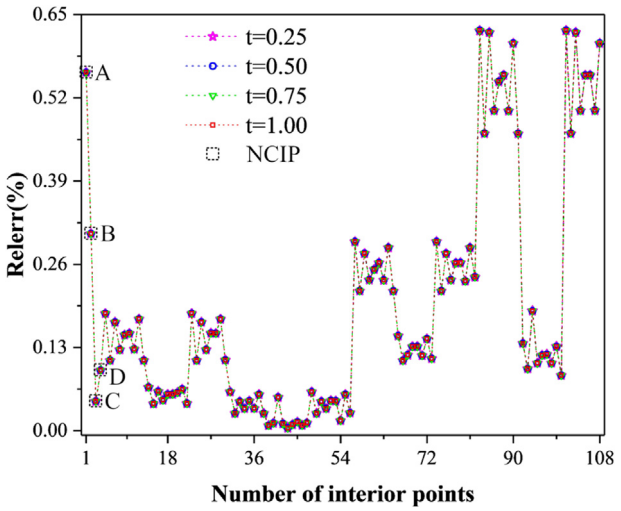

Fig. 10. The Relerr of interior points.

Table 9
The knot vector information of aircraft model.

Direction	Order	Knot vector
ξ	$p = 2$	{0, 0, 0, 1, 1, 2, 2, 3, 3, 4, 5, 6, 6, 7, 7, 8, 8, 9, 9, 10, 10, 11, 11, 12, 12, 13, 13, 14, 14, 15, 15, 16, 16, 17, 17, 18, 18, 19, 19, 20, 20, 20}
η	$q = 2$	{0, 0, 0, 1, 1, 2, 2, 2.5, 3, 3, 4, 4, 4.5, 5, 5, 6, 6, 7, 7, 7.5, 8, 8, 9, 9, 9.5, 10, 10, 11, 11, 12, 12, 13, 13, 13}

It can be seen from Table 10 that adopting NURBS interpolation can obtain relatively accurate results. The e_{L_2} stays at the same magnitude for considering with CP-ABIP and CP. Also, the Mrelerr is basically consistent using Fig. 13(a) and (b). The computer information used in the calculation process is Dell OptiPlex 7060, CPU: Core

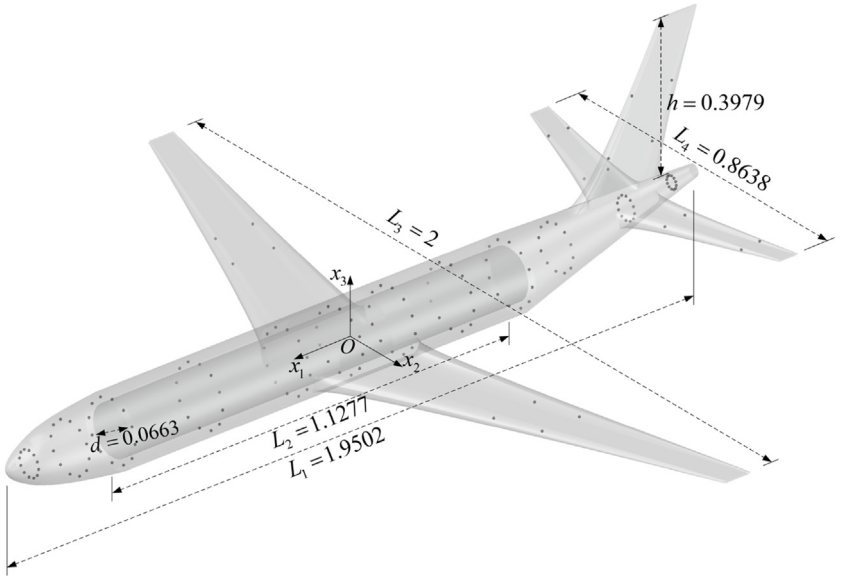

Fig. 11. Established geometry model using NURBS. L_1: the length of the fuselage; L_2: the length of cylindrical cavity inside fuselage; L_3: the wingspan width of aircraft; L_4: the tailplane width of aircraft; h: the vertical tail height of aircraft; d: the diameter of a cylindrical cavity.

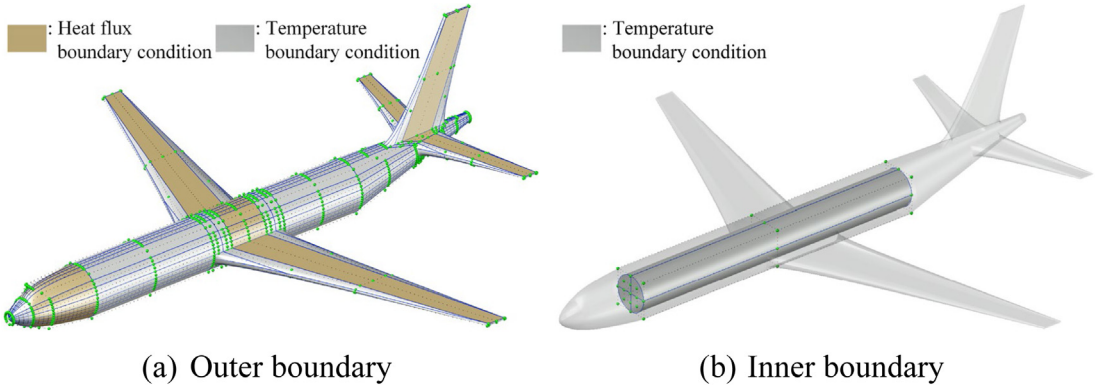

Fig. 12. The distribution of control points, elements and loads.

Table 10
The errors of numerical results corresponding to the case of the CP-ABIP and CP.

Time	e_{L_2} with CP-ABIP	e_{L_2} with CP	Mrelerr (%) with CP-ABIP	Mrelerr (%) with CP
$t = T_p/6$	5.4847e−4	4.3487e−4	0.6538	0.6534
$t = T_p/3$	5.4838e−4	4.3472e−4	0.6534	0.6530
$t = T_p/2$	5.4840e−4	4.3478e−4	0.6535	0.6531

I7-8700, 32G of memory. The CPU time to calculate the temperature field at one moment is 0.3906s with CP-ABIP. Therefore, the presented postprocessing scheme is feasible.

It can be seen from Eq. (50) that the temperature field presents a period of change with $T_p = 2\pi/5$, where T_p denotes the period of temperature change. In this example, $t \in [0, T_p/2]$ is carried out, where the time step $\Delta t = T_p/120 \approx 0.105$ is adopted. Fig. 14 gives the contours of temperature and temperature relative error at

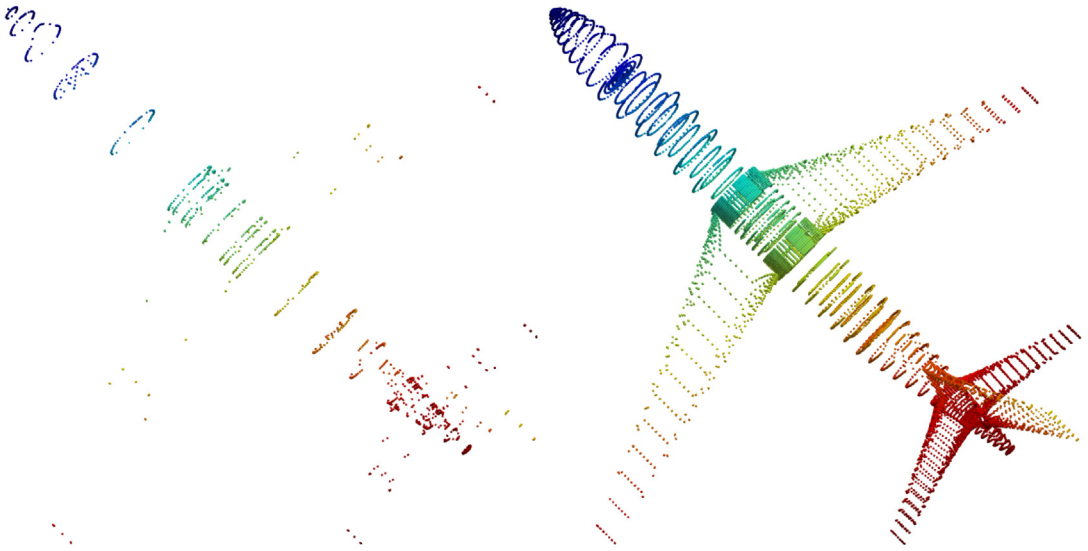

(a) 1146 CP. (b) 1146 CP and 20794 ABIP (CP-ABIP).

Fig. 13. The points of computation temperature including collocation points (CP) on the inner and outside boundaries and the added boundary-element interpolation points (ABIP).

different times using CP-ABIP. From the distribution of temperature error, it can be seen that the relative errors of the calculation points of the whole structure remain very stable at different times.

7. Conclusions

In this paper, IG-DRBEM is firstly applied to analyze the transient heat conduction of FGMs, and stable and accurate numerical results are obtained. The classical DRM is used to transform domain integral into boundary integral, which maintains the advantages of dimension reduction of BEM to some extent. Due to the non-uniform characteristics of FGMs, an additional domain integral term that does not exist when dealing with homogeneous materials appears in the boundary-domain integral equation, as shown in the last term on the right of Eq. (10). This domain integral term needs special treatment because its denominator is a function of the distance between two points, as shown in Eq. (38). An approach introduced by this paper similar to the rigid body displacement method of traditional BEM is used to calculate the matrix elements accurately. DRM is a widely used domain integral transformation method. The coupling of DRBEM and isogeometric methods greatly enhance the application scope of IGBEM. The realization of numerical examples shows that the IG-DRBEM has the following advantages: (1) After CAD modeling is completed, the control point and knot vector information can be directly extracted for numerical analysis, realizing the seamless connection between CAD and CAE; (2) After the solution is completed, the temperature at any point in the domain and at any point on the element can be solved according to user needs, where the temperature at any point on the element can be obtained by NURBS interpolation, which to some extent makes up for the solution of temperature field at non-collocation points on large-size elements; (3) The framework of the present method in this paper is based on the 3D steady-state potential IGBEM theory in literature [21]. The IG-DRBEM in this paper still maintains a good ability to solve the nearly singular integral, so as to solve the temperature field in the near boundary of the domain more accurately.

The solution models adopted in this paper are single patch modeling, which limits the geometric complexity of the solution problem to a certain extent. But there are still some complex geometries that can be realized by increasing the number of control points and adjusting the positions and weights of control points based on the simple single patch NURBS models just like the ellipsoid or torus. However, in order to be able to analyze more complex geometric models in the future multi-patch modeling is needed. The main difficulty in analyzing the multi-patch

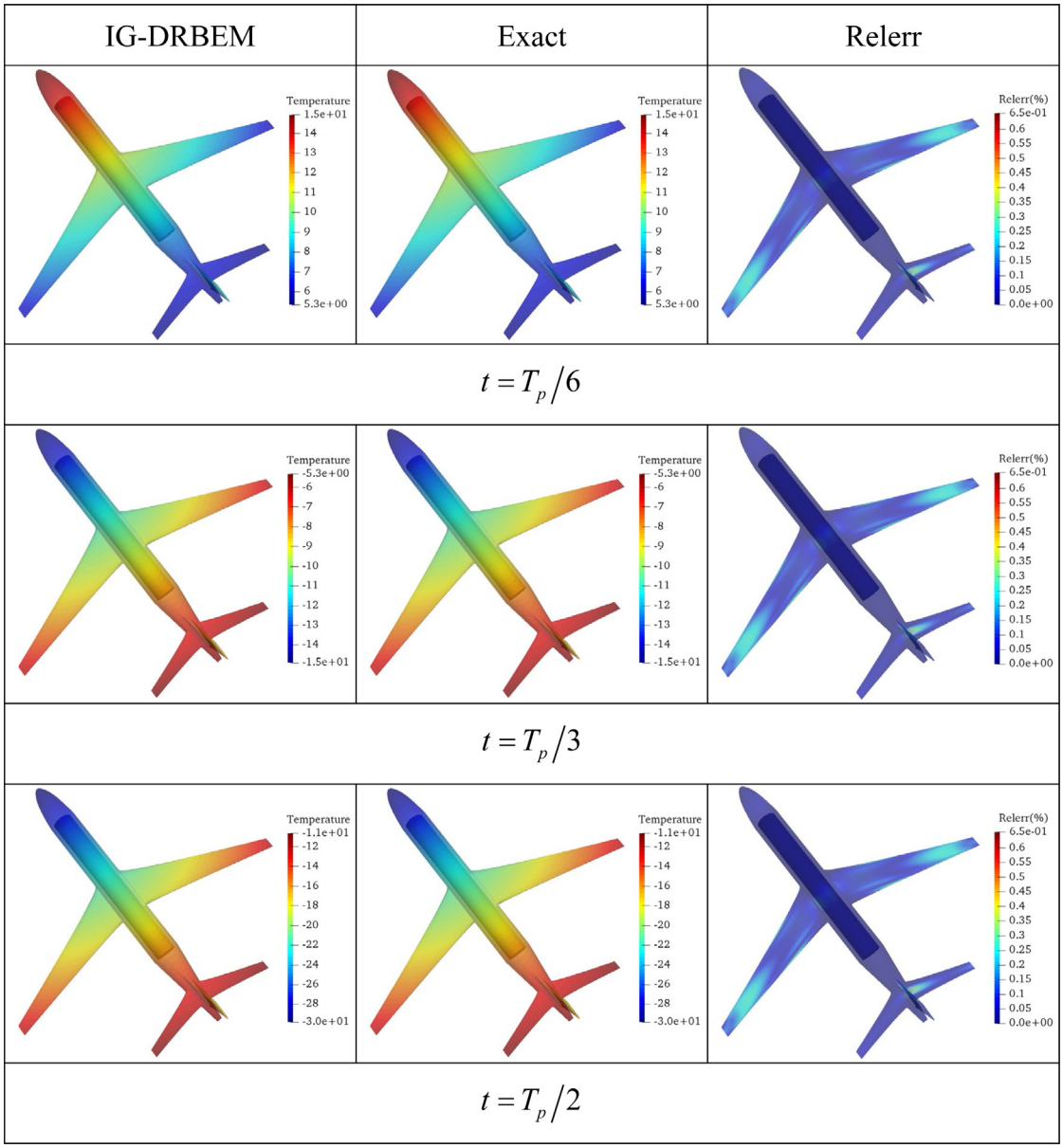

Fig. 14. Contour of temperature and temperature relative error at different times using CP-ABIP.

stitching model is that the overlapped nodes of adjacent patches cause the non-positive definite coefficient matrices. These works will be considered systematically in the future. In addition, this paper approximates geometry and field quantities based on the NURBS basis function, which cannot realize element adaptive refinement. T-splines or other appropriate methods will be utilized in the future to solve this problem.

Declaration of competing interest

The authors declare that they have no known competing financial interests or personal relationships that could have appeared to influence the work reported in this paper.

Acknowledgments

The research was supported by the National Natural Science Foundation of China (Nos. 11872166, 11972143). I would like to thank Elena Atroshchenko from the University of New South Wales for her suggestion when I first started my research on IG-DRBEM.

References

[1] R.N. Simpson, S.P.A. Bordas, J. Trevelyan, T. Rabczuk, A two-dimensional isogeometric boundary element method for elastostatic analysis, Comput. Methods Appl. Mech. Engrg. 209–212 (2012) 87–100.
[2] T.J. Hughes, J.A. Cottrell, Y. Bazilevs, Isogeometric analysis: CAD, finite elements, NURBS, exact geometry and mesh refinement, Comput. Methods Appl. Mech. Engrg. 194 (39–41) (2005) 4135–4195.
[3] L. Piegl, W. Tiller, Curve and surface constructions using rational B-splines, Comput. Aided Des. 19 (9) (1987) 485–498.
[4] M.A. Scott, R.N. Simpson, J.A. Evans, S. Lipton, S.P.A. Bordas, T.J.R. Hughes, T.W. Sederberg, Isogeometric boundary element analysis using unstructured T-splines, Comput. Methods Appl. Mech. Engrg. 254 (2013) 197–221.
[5] M.J. Peake, J. Trevelyan, G. Coates, Extended isogeometric boundary element method (XIBEM) for two-dimensional Helmholtz problems, Comput. Methods Appl. Mech. Engrg. 259 (2013) 93–102.
[6] R.N. Simpson, M.A. Scott, M. Taus, D.C. Thomas, H. Lian, Acoustic isogeometric boundary element analysis, Comput. Methods Appl. Mech. Engrg. 269 (2014) 265–290.
[7] S. Keuchel, N.C. Hagelstein, O. Zaleski, O. von Estorff, Evaluation of hypersingular and nearly singular integrals in the isogeometric boundary element method for acoustics, Comput. Methods Appl. Mech. Engrg. 325 (2017) 488–504.
[8] A.I. Ginnis, K.V. Kostas, C.G. Politis, P.D. Kaklis, K.A. Belibassakis, Th.P. Gerostathis, M.A. Scott, T.J.R. Hughes, Isogeometric boundary-element analysis for the wave-resistance problem using T-splines, Comput. Methods Appl. Mech. Engrg. 279 (2014) 425–439.
[9] G. Beer, B. Marussig, J. Zechner, C. Dünser, T.-P. Fries, Isogeometric boundary element analysis with elasto-plastic inclusions. Part 1: plane problems, Comput. Methods Appl. Mech. Engrg. 308 (2016) 552–570.
[10] G. Beer, V. Mallardo, E. Ruocco, B. Marussig, J. Zechner, C. Dünser, T.-P. Fries, Isogeometric boundary element analysis with elasto-plastic inclusions. Part 2: 3-D problems, Comput. Methods Appl. Mech. Engrg. 315 (2017) 418–433.
[11] B.H. Nguyen, H.D. Tran, C. Anitescu, X. Zhuang, T. Rabczuk, An isogeometric symmetric Galerkin boundary element method for two-dimensional crack problems, Comput. Methods Appl. Mech. Engrg. 306 (2016) 252–275.
[12] X. Peng, E. Atroshchenko, P. Kerfriden, S.P.A. Bordas, Isogeometric boundary element methods for three dimensional static fracture and fatigue crack growth, Comput. Methods Appl. Mech. Engrg. 316 (2017) 151–185.
[13] F.L. Sun, C.Y. Dong, H.S. Yang, Isogeometric boundary element method for crack propagation based on Bézier extraction of NURBS, Eng. Anal. Bound. Elem. 99 (2019) 76–88.
[14] Z.L. Han, C.Z. Cheng, S.L. Yao, Z.R. Niu, Determination of stress intensity factors of V-notch structures by characteristic analysis coupled with isogeometric boundary element method, Eng. Fract. Mech. 222 (2019) 106717.
[15] T. Takahashi, T. Yamamoto, Y. Shimba, H. Isakari, T. Matsumoto, A framework of shape optimisation based on the isogeometric boundary element method toward designing thin-silicon photovoltaic devices, Eng. Comput. 35 (2019) 423–449.
[16] L.L. Chen, H. Lian, Z. Liu, H.B. Chen, E. Atroshchenko, S.P.A. Bordas, Structural shape optimization of three dimensional acoustic problems with isogeometric boundary element methods, Comput. Methods Appl. Mech. Engrg. 355 (2019) 926–951.
[17] M. Yoon, J. Lee, B. Koo, Shape design optimization of thermoelasticity problems using isogeometric boundary element method, Adv. Eng. Softw. 149 (2020) 102871.
[18] S. Li, J. Trevelyan, Z. Wu, H. Lian, D. Wang, W. Zhang, An adaptive SVD–Krylov reduced order model for surrogate based structural shape optimization through isogeometric boundary element method, Comput. Methods Appl. Mech. Engrg. 349 (2019) 312–338.
[19] L.L. Chen, C. Lu, H.J. Lian, Z.W. Liu, W.C. Zhao, S.Z. Li, H.B. Chen, S.P.A. Bordas, Acoustic topology optimization of sound absorbing materials directly from subdivision surfaces with isogeometric boundary element methods, Comput. Methods Appl. Mech. Engrg. 362 (2020) 112806.
[20] H.L. Oliveira, H.D.C. e Andrade, E.D. Leonel, An isogeometric boundary element approach for topology optimization using the level set method, Appl. Math. Model. 84 (2020) 536–553.
[21] Y.P. Gong, C.Y. Dong, An isogeometric boundary element method using adaptive integral method for 3D potential problems, J. Comput. Appl. Math. 319 (2017) 141–158.
[22] Z.L. An, T.T. Yu, T.Q. Bui, C. Wang, N.A. Trinh, Implementation of isogeometric boundary element method for 2-D steady heat transfer analysis, Adv. Eng. Softw. 116 (2018) 36–49.
[23] B. Yu, G.Y. Cao, W.D. Huo, H.L. Zhou, E. Atroshchenko, Isogeometric dual reciprocity boundary element method for solving transient heat conduction problems with heat sources, J. Comput. Appl. Math. 385 (2021) 113197.
[24] D. Nardini, C.A. Brebbia, A new approach to free vibration using boundary elements, Bound. Elem. Methods Engrg. (1982).
[25] P.W. Partridge, C.A. Brebbia, L.C. Wrobel, The Dual Reciprocity Boundary Element Method, Computational Mechanics Publications, Southampton, Boston, 1992.
[26] A.J. Nowak, C.A. Brebbia, The multiple-reciprocity method. A new approach for transforming BEM domain integrals to the boundary, Eng. Anal. Bound. Elem. 6 (3) (1989) 164–167.
[27] Y. Ochiai, T. Sekiya, Steady heat conduction analysis by improved multiple-reciprocity boundary element method, Eng. Anal. Bound. Elem. 18 (2) (1996) 111–117.

[28] M.S. Ingber, A triple reciprocity boundary element method for transient heat conduction analysis, WIT Trans. Model. Simul. 8 (1994) 41–49.
[29] Y. Ochiai, Two-dimensional unsteady heat conduction analysis with heat generation by triple-reciprocity BEM, Internat. J. Numer. Methods Engrg. 51 (2) (2001) 143–157.
[30] Y. Ochiai, Y. Kitayama, Three-dimensional unsteady heat conduction analysis by triple-reciprocity boundary element method, Eng. Anal. Bound. Elem. 33 (6) (2009) 789–795.
[31] X.W. Gao, The radial integration method for evaluation of domain integrals with boundary-only discretization, Eng. Anal. Bound. Elem. 26 (10) (2002) 905–916.
[32] C. Xu, C.Y. Dong, R. Dai, RI–IGABEM based on PIM in transient heat conduction problems of FGMs, Comput. Methods Appl. Mech. Engrg. 374 (2021) 113601.
[33] J.P. Agnantiaris, D. Polyzos, D.E. Beskos, Three-dimensional structural vibration analysis by the dual reciprocity BEM, Comput. Mech. 21 (1998) 372–381.
[34] E.L. Albuquerque, P. Sollero, P. Fedelinski, Dual reciprocity boundary element method in Laplace domain applied to anisotropic dynamic crack problems, Comput. Struct. 81 (17) (2003) 1703–1713.
[35] S.H. Javaran, N. Khaji, H. Moharrami, A dual reciprocity BEM approach using new fourier radial basis functions applied to 2D elastodynamic transient analysis, Eng. Anal. Bound. Elem. 35 (1) (2011) 85–95.
[36] B. Yu, H.L. Zhou, H.L. Chen, Y. Tong, Precise time-domain expanding dual reciprocity boundary element method for solving transient heat conduction problems, Int. J. Heat Mass Transfer 91 (2015) 110–118.
[37] X.W. Gao, T.G. Davies, Boundary Element Programming in Mechanics, Camberidge University Press, 2002.
[38] Y.M. Zhang, Y.P. Gong, X.W. Gao, Calculation of 2D nearly singular integrals over high-order geometry elements using the sinh transformation, Eng. Anal. Bound. Elem. 60 (2015) 144–153.
[39] G.Z. Xie, J.M. Zhang, Y.Q. Dong, C. Huang, G.Y. Li, An improved exponential transformation for nearly singular boundary element integrals in elasticity problems, Int. J. Solids Struct. 51 (6) (2014) 1322–1329.
[40] Y. Gu, Q. Hua, W. Chen, C. Zhang, Numerical evaluation of nearly hyper-singular integrals in the boundary element analysis, Comput. Struct. 167 (2016) 15–23.
[41] X.Y. Qin, J.M. Zhang, G.Z. Xie, F.L. Zhou, G.Y. Li, A general algorithm for the numerical evaluation of nearly singular integrals on 3D boundary element, J. Comput. Appl. Math. 235 (14) (2011) 4174–4186.
[42] J.C.F. Telles, A self-adaptive coordinate transformation for efficient numerical evaluation of general boundary element integrals, Internat. J. Numer. Methods Engrg. 24 (1987) 959–973.
[43] G. Karami, D. Derakhshan, An efficient method to evaluate hypersingular and supersingular integrals in boundary integral equations analysis, Eng. Anal. Bound. Elem. 23 (4) (1999) 317–326.
[44] Z.R. Niu, X.X. Wang, H.L. Zhou, C.L. Zhang, A novel boundary integral equation method for linear elasticity-natural boundary integral equation, Acta Mech. Solida Sin. 14 (1) (2001) 2–10.
[45] J. Wang, T.K. Tsay, Analytical evaluation and application of the singularities in boundary element method, Eng. Anal. Bound. Elem. 29 (3) (2005) 241–256.
[46] D.W. Hahn, M.N. Özisik, Heat Conduction, John Wiley & Sons, 2012.
[47] B. Yu, W.A. Yao, A precise time-domain expanding boundary-element method for solving three-dimensional transient heat conduction problems with variable thermal conductivity, Numer. Heat Transfer B 66 (5) (2014) 422–445.